

Hybrid Beamforming in 5G mmWave Networks: a Full-stack Perspective

Felipe Gómez-Cuba, *Member, IEEE*, Tommaso Zugno, *Student Member, IEEE*,
Junseok Kim, *Member, IEEE*, Michele Polese, *Member, IEEE*,
Saewoong Bahk, *Senior member, IEEE*, Michele Zorzi, *Fellow, IEEE*

Abstract

This paper studies the cross-layer challenges and performance of Hybrid Beamforming (HBF) and Multi-User Multiple-Input Multiple-Output (MU-MIMO) in 5G millimeter wave (mmWave) cellular networks with full-stack TCP/IP traffic and MAC scheduling. While previous research on HBF and MU-MIMO has focused on link-level analysis of full-buffer transmissions, this work reveals the interplay between HBF techniques and the higher layers of the protocol stack. To this aim, prior work on full stack simulation of mmWave cellular network has been extended by including the modeling of MU-MIMO and HBF. Our results reveal novel relations between the networking layers and the HBF MU-MIMO performance in the physical layer. Particularly, throughput can be increased in 5G networks by means of Spatial Division Multiple Access (SDMA). However, in order to achieve such benefits it is necessary to take into account certain trade-offs and the implementation complexity of a full-stack HBF solution.

Index Terms

mmWave, hybrid beamforming, 3GPP NR, end-to-end, simulations

Felipe Gómez-Cuba is with AtlantTIC, University of Vigo, Spain. Email: gomezcuba@gts.uvigo.es.

Tommaso Zugno and Michele Zorzi are with the Department of Information Engineering, University of Padova, Padova, Italy. Email: {zugnotom, zorzi}@dei.unipd.it

Junseok Kim is with System LSI, Samsung Electronics, Gyeonggi-do, South Korea. Email: junseok.kim@samsung.com.

Michele Polese is with the Institute for the Wireless Internet of Things, Northeastern University, Boston, MA USA. Email: m.polese@northeastern.edu.

Saewoong Bahk is with the Department of ECE and INMC, Seoul National University, Seoul, South Korea. Email: sbahk@snu.ac.kr.

I. INTRODUCTION

The next generations of mobile networks will need to satisfy the capacity, latency, and reliability demands of present and future networked applications [1]. On one hand, the connected society is heavily relying on wireless networks to consume a wide range of digital services, from video streaming to cloud storage, which require high capacity links. On the other hand, remote control applications for smart factories and eHealth introduce high reliability and low latency constraints. To satisfy the wide range of use cases, the design of flexible and highly performing 5G and beyond cellular networks is of primary importance [2], [3].

To this end, the 3rd Generation Partnership Project (3GPP) has recently defined a set of specifications for 3GPP NR [4], a new Radio Access Network (RAN) architecture that includes several technological advancements with respect to previous generations [2]. It features a flexible frame structure, in which the parameters of the Orthogonal Frequency Division Multiplexing (OFDM) numerology can be tuned to support different services, and, for the first time, the possibility of using the millimeter wave (mmWave) spectrum in the radio access. Releases 15 and 16, indeed, support carrier frequencies up to 52.6 GHz, with possible extensions to 71 GHz planned for Release 17 [5].

The mmWave spectrum is a promising technological enabler that can provide high capacity links, thanks to the wide availability of bandwidth, which would help combating the spectrum crunch of traditional sub-6 GHz bands [6]. NR will thus be capable of exploiting much larger bandwidths with respect to previous 3GPP waveforms, with up to 400 MHz for each carrier [4]. Another feature that mmWaves introduce is the possibility of packing a large number of antenna elements in a small form factor, both in base stations and in mobile devices. This makes it possible to focus the energy of the transmission in narrow beams, and to offset the increase in path loss (due to the higher carrier frequency) with a higher Beamforming (BF) gain [7]. Different BF architectures have also been considered in the literature. With analog BF, the transceivers are equipped with a single Radio Frequency (RF) chain, and a single beam is generated using analog phase shifters in the N antenna elements of the phase array. More advanced transceivers use hybrid or digital BF architectures, with $K \leq N$ RF chains. While increasing the complexity and power consumption of the device, they enable a finer control on the BF process, which can be based on combined digital and analog processing [8].

Hybrid and digital BF architectures, therefore, are capable of steering multiple beams from

a single antenna array, with (possibly) independent data streams, effectively enabling Multi-User Multiple-Input Multiple-Output (MU-MIMO) operations at mmWaves [7]. As a result, this makes it possible to increase the spectral efficiency of the network, as different users can be served with Spatial Division Multiple Access (SDMA) in the same time and frequency resources. Hybrid Beamforming (HBF) solutions, in particular, are considered as a cost- and energy-effective solution for MU-MIMO at mmWaves, and have been practically implemented and deployed in commercial devices [9].

A. Contributions

The specifications for 3GPP NR natively consider the possibility of MU-MIMO transmissions, and embed a beam management framework to support directional transmissions [10]. However, despite the promising features of HBF at mmWaves, the state of the art currently lacks an analysis of how a *physical layer* based on HBF interacts with the *full protocol stack*, from the Medium Access Control (MAC) layer, e.g., for scheduling, to the transport layer and applications.

To fill this gap, in this paper we present an analysis of how HBF techniques can be integrated in the protocol stack of 5G and beyond cellular networks, focusing on optimal beam design and scheduling strategies for different scenarios and applications. To the best of our knowledge, this is the first contribution that performs an end-to-end evaluation of the potential and challenges of MU-MIMO HBF with a full-stack perspective. Notably, we

- provide a tutorial on how the protocol stack in 3GPP NR supports MU-MIMO, in terms of basic signaling and operations, with references to the relevant technical specifications;
- propose two Minimum Mean Squared Error (MMSE) HBF design strategies for MU-MIMO in 3GPP NR, comparing approaches which present a trade-off between complexity and performance, and how they can be practically integrated in the 5G protocol stacks;
- unravel the sub-optimal interaction that may arise from the combination of sophisticated MU-MIMO HBF strategies and traditional MAC scheduling strategies, which do not fully support SDMA over independent beams. We then propose scheduling strategies which, while being standard compliant, improve the performance of MU-MIMO communications;
- present the results of an extensive simulation campaign, based on our novel implementation of HBF MU-MIMO transmissions in the ns-3 mmWave module [11]. To the best of our

knowledge, this tool¹ is the first open source software to support the simulation of HBF MU-MIMO at mmWaves, with a 3GPP-like protocol stack, the 3GPP channel model for mmWave frequencies, and, thanks to the integration with ns-3, the TCP/IP stack and realistic applications. Our results show that HBF can improve the performance of a saturated, single-layer mmWave network, for a variety of end-to-end traffic flows, and that an HBF-aware scheduling design is fundamental to achieve the potential gains of multi-layer solutions.

B. State of the Art

MU-MIMO channels have received considerable academic interest since the 90s [12]. This interest increased even further as the number of antennas per device grew, harnessing the advantages of *massive Multiple-Input Multiple-Output (MIMO)* [13]. Nowadays MU-MIMO with very large antenna arrays is an integral part of the 5G NR cellular standard published by the 3GPP [14]–[16]. MU-MIMO pilots, channel estimation and feedback procedures in the standard are concisely described in [17]. Signal processing techniques for mmWave systems are reviewed in [18]. Beam-management procedures in 5G are covered in [10]. Moreover, the research community has widely studied efficient transceiver architectures [19], and beam design strategies [8], and has characterized the performance gains that MU-MIMO and SDMA can yield in mmWave deployments [20].

The research community has also recently focused on the evaluation of the end-to-end performance of 5th generation (5G) mmWave networks, with analysis [21], simulations [22], and experiments [23]. This has been recognized as fundamental to enable a proper design and validation of 5G technologies, given that new, unexplored technologies are being coupled with protocols and networks that have not been specifically designed for NR [11]. For example, the authors of [24] investigate how Transmission Control Protocol (TCP) behaves on top of mmWave links, highlighting pitfalls and strategies to improve the overall performance. The state of the art, however, has mostly focused on the interaction between the higher layer of the protocol stack and a physical layer with analog BF [25]. Some evaluations are available for HBF at mmWaves, but focus on simplified full-buffer link-layer evaluations [8], [19], [20], [26]. Similarly, performance analysis of digital BF schemes for 3GPP NR has focused on power consumption and control procedures [10], [27].

¹Available at <https://github.com/signetlabdei/ns3-mmwave-hbf>

As discussed in the previous paragraphs, this paper advances the state of the art by jointly analyzing HBF design and higher layer issues, to understand how their interplay can be optimized to maximize the performance of the network.

C. Paper Structure

The remainder of the paper is organized as follows. Sec. II discusses HBF and scheduling design in 3GPP NR networks. Sec. III, then, describes the performance evaluation results, and Sec. IV concludes the paper, providing suggestions for future research directions.

II. FULL-STACK INTEGRATION OF HBF FOR MMWAVES

This section describes how the NR protocol stack is designed to support HBF (Sec. II-A), reviews HBF design strategies (Sec. II-B), and analyzes the challenges associated with the interplay between HBF and schedulers, proposing different HBF-aware scheduling policies (Sec. II-C).

A. HBF in the 3GPP NR Stack

The 3GPP 5G standard specifies the NR waveform and conformance requirements for devices [14], [28]. The interface between the waveform and the antenna array is standardized through a series of “antenna ports.” The details of BF operations applied to signals in each port are left to the vendor implementation, and constrained only by conformance requirements such as those in [28].

In the NR waveform, complex symbols are mapped in a 3-dimensional OFDM resource grid comprising the OFDM symbol number in time (n), the OFDM subcarrier number in frequency (k), and the *SDMA layer* number (ℓ) [14, Table 7.3.1.3-1]. Furthermore, layers can be mapped to more than one antenna port (p) using several precoding configurations [14]. These antenna ports are defined as signal input/output interfaces to the antenna array. The mapping of antenna ports to actual antenna elements may be vendor-specific, but must guarantee that in the same port and within the same “slot” of 14 consecutive OFDM symbols, the channel may be inferred through DeModulation Reference Signals (DMRSs) that are orthogonal and specific in each port [15]. We note that the standard does not mandate that each port corresponds to a frequency-flat analog beam, in other words, further vendor-specific frequency-selective HBF operations can be considered.

At the NR MAC layer, the scheduler assigns radio Resource Blocks (RBs) in the grid with indices (n, k, ℓ) . The broadest time division are *frames* of 10 ms duration. Each frame is divided in 10 *subframes* of 1 ms. These large scale time units are similar to Long Term Evolution (LTE), and can admit either Time Division Duplexing (TDD) or Frequency Division Duplexing (FDD) configurations. However, differently from LTE, slots in any subframe can be labeled as Downlink (DL), Uplink (UL) or *flexible*, where the latter represent an innovation in 5G that permits the scheduler to dynamically change the DL/UL division over consecutive subframes.

In the smaller time-scale of the OFDM signal, the dimensions of the time-frequency grid depend on the fundamental *numerology* parameter $\mu \in \{0, 1, 2, 3, 4\}$. OFDM symbols are grouped in *slots* of 14 symbols, such that each subframe has 2^μ slots. The inter-carrier spacing is $\Delta f = 2^\mu \times 15$ kHz, and each OFDM symbol's duration is $\frac{2^{-\mu}}{14}$ ms. The maximum bandwidth without carrier aggregation is 400 MHz. In addition, the smallest scheduling granularity in NR is the “mini-slot,” which can be only 2 OFDM symbols long and does not necessarily have to be time-aligned with multiples of the nominal slot start instants. This allows NR schedulers to assign “asynchronous” transmissions that do not start at the same time. Moreover, parallel resource grids are defined simultaneously for each port p **and for each numerology** μ , meaning that it is possible to schedule contiguous transmissions with different physical layer parameters in the same frame.

The NR versatile waveform supports different frequencies, from the conventional 700 MHz–6 GHz spectrum up to the 24 – 70 GHz mmWave spectrum. As a result, some NR options are not useful when operating at mmWaves. One is Orthogonal Frequency Division Multiple Access (OFDMA), since highly directive mmWave BF typically requires frequency-flat analog operations. This means that the radio device cannot apply different analog beams to different subcarriers of the same OFDM symbol. Therefore, in mmWave all subcarriers k in a port-symbol pair need to be assigned to the same user. As a consequence, scheduling in mmWave NR reduces to a 2-dimension Time Division Multiple Access (TDMA) and SDMA grid (n, ℓ) . The second is the use of SDMA transmissions with more than one layer to the same user, since typical mmWave MIMO channel matrices are rank deficient (i.e., the second largest eigenvalue is much smaller than the first) [7]. In turn, multiple transmissions with rank ≥ 2 to the same user are ineffective, thus SDMA can only be implemented as a MU-MIMO technique, but not as a single user MIMO technique.

B. HBF Design

We assume that simultaneous SDMA transmissions are allocated into different layers ℓ . The channel matrix between the Base Station (BS) and each User Equipment (UE) u is denoted by $\mathbf{H}_u[n, k]$ in OFDM symbol n and subcarrier k . In DL, the BS selects a wideband analog BF vector for each transmit layer \mathbf{v}_ℓ using some BF scheme, and the UE receives with the analog BF vector \mathbf{w}_u . Thus the *effective* scalar complex channel between the transmit layer ℓ and the receive antenna port of the UE is given by

$$h_{eq}[u, \ell, n, k] = \mathbf{w}_u^T \mathbf{H}_u[n, k] \mathbf{v}_\ell,$$

and the UL channel is computed with the transposed channel matrix and swapping transmitter and receiver beamforming vectors, resulting in the same complex scalar number.

We follow a Signal to Interference plus Noise Ratio (SINR)-based point-to-point link performance model. This means that we obtain an expression for the SINR of each link, assume that simultaneous links are decoded separately, and map the SINR of each link to the Block Error Rate (BLER) of the associated transmission. This is a simplification of real decoding hardware that makes the simulation of a large network tractable. Real NR demodulation and decoding may use sophisticated joint decoding such as MU-MIMO sphere decoding [29], combined with the LDPC and Polar channel codes of each transmission [14].

For multiple simultaneous downlink transmissions sent by the BS on multiple layers, we write the DL SINR of user u at subcarrier k as a function of the effective channel gains as

$$SINR_u^{DL}[k] = \frac{L_u |h_{eq}[u, \ell(u), n, k]|^2 P/K}{\sum_{u' \neq u} L_u |h_{eq}[u, \ell(u'), n, k]|^2 P/K + \Delta f N_o} \quad (1)$$

where K is the number of subcarriers, L_u is the pathloss of user u , P/K is the BS transmitted power per layer equally divided among all subcarriers, N_o is the noise Power Spectral Density (PSD) and Δf is the inter-carrier spacing. For the discussion of BF design at a single BS, we evaluate the sum of interference only over UEs connected to the same BS, producing self-interference. If there are other BSs in the scenario, their BF design is independent and their interference may be written as a constant in addition to N_o . We note that the self-interference terms correspond to “mismatched” beams, i.e., an interfering signal is received by user u through the channel of user u but it was sent by the transmitter layer $\ell(u')$ using a BF vector designed for user u' . Usually this would mean that an interference signal’s power is lower than the desired

signal power. Still, this interference term may be significantly stronger than the noise, and thus the link SINR will be much lower than the Signal to Noise Ratio (SNR).

In UL self-interference is even more severe because the UL SINR expression is in turn

$$SINR_u^{UL}[k] = \frac{L_u |h_{eq}[u, \ell(u), n, k]|^2 P}{\sum_{u' \neq u} L_{u'} |h_{eq}[u', \ell(u), n, k]|^2 P + \Delta f N_o}, \quad (2)$$

where the layer assigned to user u receives the interference signal of layer $\ell(u')$ through the channel of user u' . In other words, pathloss gains in the denominator $L_{u'}$ are also mismatched. Since the pathloss gain of an interferer might occasionally be much greater than the pathloss gain of the desired signal L_u , BF alone is not enough to guarantee that the interference power is lower than the desired signal power in UL as it was in DL. For example this would happen in a layer that is receiving from a user far from the BS that is coexisting with a nearby user in another layer.

Under our SINR point-to-point link model, we propose the following design methods to obtain BF vectors to achieve good link SNR or SINR values in (1) and (2). Our BF designs extend beyond the standard precoding tables [14], but they can be implemented within the vendor-specific part of the BF system, where ports are mapped to antenna elements:

1) *Geometric BeamForming (GBF)*: We denote the antenna array response as a function $\mathbf{a}(\theta, \phi)$ that depends on the angles of azimuth and elevation (θ, ϕ) . For example, in a Uniform Planar Array (UPA) with $N_1 \times N_2$ antennas separated half a wavelength, the i -th coefficient of this vector would be

$$a_i(\theta, \phi) = e^{-j\frac{\pi}{2}((i \bmod N_1) \sin(\theta) + \lfloor i/N_1 \rfloor \sin(\phi))},$$

whereas other expressions would give $\mathbf{a}(\theta, \phi)$ for other antenna array shapes.

Notably, in the UPA and other array shapes where $\mathbf{a}(\theta, \phi)^H \mathbf{a}(0, 0) = \mathbf{a}(0, 0)^H \mathbf{a}(-\theta, -\phi)$, we can easily adopt the vector $\mathbf{a}(\theta, \phi)^H$ to design a beam that points in the direction (θ, ϕ) . In geometric BF, the vectors are simply selected by pointing the array in the physical direction between the BS position and the UE position. That is, if the position coordinates are (x_{BS}, y_{BS}, z_{BS}) and

(x_u, y_u, z_u) , then we have

$$\begin{aligned}
\theta_D &= \arctan \frac{y_u - y_{BS}}{x_u - x_{BS}} + \pi \mathbb{I}_{(x_u < x_{BS})} \quad \text{mod } 2\pi \\
\phi_D &= \arctan \frac{z_u - z_{BS}}{\sqrt{(y_u - y_{BS})^2 + (x_u - x_{BS})^2}} \\
\theta_A &= \theta_D + \pi \\
\phi_A &= -\phi_D \\
\mathbf{v}_{\ell(u)}^T &= \mathbf{a}(\theta_D, \phi_D)^H \\
\mathbf{w}_u^T &= \mathbf{a}(\theta_A, \phi_A)^H
\end{aligned} \tag{3}$$

where $\mathbb{I}_{(e)}$ is the indicator function for event e , the subindex D indicates the angles of departure, subindex A indicates the angles of arrival, and the subindex $\ell(u)$ indicates the layer assigned to the transmission to UE u .

Finally, GBF vectors are analog, so layers are matched one-to-one with array ports in this scheme. A potential shortcoming of this BF model is that it does not adapt to changes in the channel matrix. The strongest channel gain associated with $\mathbf{H}_u[n, k]$ is represented by its largest singular value and associated eigenvectors, which could be significantly different from the physical geometric direction between the devices, especially in NLOS channels.

2) *Codebook BeamForming (CBF)*: We denote a *BF codebook* \mathcal{B} as a small collection of possible BF vectors (either because of array hardware limitations or because the feedback is limited to a $\log_2|\mathcal{B}|$ bit message). The transmitter sends reference signals using all the vectors in \mathcal{B}_D , and the receiver tests decoding the reference signals with all vectors in \mathcal{B}_A . Finally, the receiver chooses a pair of vectors from each codebook based on the observations. For example, the receiver may choose the vectors that result in the maximum empirically-observed reference signal power. In our implementation we assume the following ideal max-SNR criterion

$$\mathbf{v}_{\ell(u)}, \mathbf{w}_u = \arg \max_{\mathbf{v} \in \mathcal{B}_D, \mathbf{w} \in \mathcal{B}_A} |\mathbf{w}_u^T \mathbf{H}_u[n, k_{ref}] \mathbf{v}_\ell|^2, \tag{4}$$

where k_{ref} is a single subcarrier index where we assume a narrowband reference signal is carried. Finally, the receiver would only need to send to the transmitter a beam indicator message describing the index that $\mathbf{v}_{\ell(u)}$ occupies in the look-up table containing \mathcal{B}_D .

Codebook BF vectors are analog and layers are matched one-to-one with array ports, as in GBF. Thanks to the use of a simple codebook-lookup technique, feedback overhead would be very low. A potential drawback is that by using a single-subcarrier reference $|\mathbf{w}_u^T \mathbf{H}_u[n, k_{ref}] \mathbf{v}_\ell|^2$

the selection does not take into account the gains that would be experienced by any other subcarrier $|\mathbf{w}_u^T \mathbf{H}_u[n, k] \mathbf{v}_\ell|^2 \forall k \neq k_{ref}$. This means that only the SNR of the reference is maximized while that of other subcarriers is not. Nonetheless, due to the fact that the mmWave channel matrix is rank-deficient and the beams in the codebook are rather coarse, the SNR in different subcarriers can be quite similar and this shortcoming is not too severe.

3) *Frequency-Flat MMSE BeamForming (FMBF)*: GBF and CBF focus solely on maximizing the effective channel gains between the BS and UE u through its associated layer $\ell(u)$. This, in turn, maximizes user u 's link SNR, but does not account for interference to and from other UEs, which could result in low SINR even if the SNR is high.

Therefore, to improve the SINR, we introduce a low-complexity, low-dimensional linear matrix mapping between layers and ports, in combination with an auxiliary analog CBF underlying scheme. Let us denote the BF vectors selected using CBF by \mathbf{w}_u^{CB} and \mathbf{v}_ℓ^{CB} , and by $h_{eq}[u, p, n, k_{ref}] = (\mathbf{w}_u)^T \mathbf{H}_u[n, k_{ref}] \mathbf{v}_p$ the complex channel coefficients observed between user u and port p at the reference subcarrier k_{ref} .

We assume that first the system conducts a codebook exploration as in CBF and loads the best codebook BF vector for each user u to different antenna ports denoted $p(u)$. In addition, we assume that right after the codebook exploration the BS notifies each user of all the vectors of interest, and the receivers estimate the effective complex scalars $\sqrt{L_u} h_{eq}^{CB}[u, p(u'), n, k_{ref}]$ for all pairs $(u, p(u)')$. To report these auxiliary effective channel coefficients back to the BS, since a single reference subcarrier is used, would require $N_u^2 N_{bit}$ bits of feedback, where N_{bit} is the number of bits used to encode each complex number and N_u is the number of simultaneous users. For example in a scenario with $N_u = 4$ the feedback would be 1024 bits with high precision 32-bit floating point encoding, or 96 bits with a more aggressive 3-bit quantizer.

To simplify the notation, we assume in this section that the active users are numbered sequentially $u \in \{0 \dots N_u\}$ and that their assigned layer and port numbers are equally sequential $\ell(u) = p(u) = u$. We also omit the OFDM symbol index n . Using the auxiliary scalar channel coefficients the BS builds the following MU-MIMO reference equivalent channel matrix:

$$\mathbf{H}_{eq}[k_{ref}] = \begin{pmatrix} \sqrt{L_1} h_{eq}^{CB}[1, 1, k_{ref}] & \sqrt{L_1} h_{eq}^{CB}[1, 2, k_{ref}] & \dots & \sqrt{L_1} h_{eq}^{CB}[1, N_p, k_{ref}] \\ \sqrt{L_2} h_{eq}^{CB}[2, 1, k_{ref}] & \sqrt{L_2} h_{eq}^{CB}[2, 2, k_{ref}] & \dots & \sqrt{L_2} h_{eq}^{CB}[2, N_p, k_{ref}] \\ \vdots & \vdots & \ddots & \vdots \\ \sqrt{L_{N_u}} h_{eq}^{CB}[N_u, 1, k_{ref}] & \sqrt{L_{N_u}} h_{eq}^{CB}[N_u, 2, k_{ref}] & \dots & \sqrt{L_{N_u}} h_{eq}^{CB}[N_u, N_p, k_{ref}] \end{pmatrix} \quad (5)$$

where $N_p = N_u$ is the number of analog BF ports, each associated to a single user. Moreover since $\ell(u) = p(u) = u$, the desired channels are in the main diagonal of this matrix. Finally, on the receiver side, the receiving BF vectors would remain those of CBF, while on the transmitter side the BS designs a precoding matrix matching layers to ports by building the following MMSE DL precoding matrix

$$\mathbf{V}_{MMSE}[k_{ref}] = \mathbf{H}_{eq}^H (\mathbf{H}_{eq} \mathbf{H}_{eq}^H + \frac{N_o \Delta f}{P} \mathbf{I})^{-1}.$$

We adopt the MMSE technique because, when the noise is weak compared to the transmitted power, then $\frac{N_o \Delta f K}{P} \rightarrow 0$, and the expression converges to the pseudoinverse (zero-forcing precoder), i.e., $\mathbf{H}_{eq}[k_{ref}] \mathbf{V}_{MMSE}[k_{ref}] = \mathbf{I}$, thus suppressing the interference. In addition when the noise is strong, in the limit $\frac{N_o \Delta f K}{P} \rightarrow \infty$, the MMSE expression converges to the hermitian (matched filter) which maximizes the received SNR. Thus, MMSE offers a balance between interference suppression and noise reduction giving good SINR values for any noise-to-transmitted power ratio ($\frac{N_o \Delta f K}{P}$).

Finally, the final *effective* transmit BF vectors at the BS for DL are obtained by first computing

$$(\tilde{\mathbf{v}}_1^{MMSE} \dots \tilde{\mathbf{v}}_{N_u}^{MMSE}) = (\mathbf{v}_1^{CB} \dots \mathbf{v}_{N_u}^{CB}) \mathbf{V}_{MMSE}[k_{ref}],$$

and then introducing the following normalization to preserve the transmitted power constraint in each layer:

$$\mathbf{v}_u^{MMSE} = \tilde{\mathbf{v}}_u^{MMSE} / |\tilde{\mathbf{v}}_u^{MMSE}|.$$

Introducing these effective vectors into (1), instead of the auxiliary CBF vectors we discussed earlier, results in the new SINR values of the MMSE technique.

For UL, an equivalent hybrid combining at the BS receiver can be formulated by adopting the transpose of the matrices described above.

The FMBF technique relies solely on estimations performed at the reference subcarrier k_{ref} and is still frequency-flat. This introduces only a small amount of additional feedback as only one subcarrier equivalent matrix needs to be reported. The precoding/combining matrix is explicitly designed to improve the SINR in the reference subcarrier and, as a side effect, the SINR would improve in other subcarriers with similar equivalent channel matrices. But since FMBF does not take into account the effective channel of the other subcarriers, it does not guarantee complete interference suppression in all subcarriers.

4) *Frequency-Selective MMSE BeamForming (SMBF)*: SMBF is an HBF scheme comprising a frequency-selective low-dimensional linear matrix mapping from ports to layers, which may be different in each subcarrier, together with a codebook based frequency-flat analog beam selection to map ports to antenna array elements.

For this, in DL we need to assume that after beam codebook exploration is performed, pilot signals are transmitted in all subcarriers and the receivers can report back to the transmitter a large set of effective channel coefficients $\{h_{eq}^{CB}[u, p(u'), n, k]$ for all pairs $(u, p(u'))$ and subcarrier indices $k\}$. This would require roughly $K \times N_u^2 N_{bit}$ bits of feedback. For example if $K = 100$, for the case $N_u = 4$ and with a coarse quantizer with $N_{bit} = 3$, we could send the resulting 9.6 kbits of feedback in a single OFDM symbol, whereas using high precision complex number encoding with $N_{bit} = 32$ would be prohibitive. Using the effective channel information the transmitter builds a collection of K different equivalent channel matrices, one for each subcarrier ($\mathbf{H}_{eq}[k] \forall k \in \{1 \dots K\}$). For each subcarrier k the transmitter designs a different digital precoding matrix

$$\mathbf{V}_{MMSE}[k] = \mathbf{H}_{eq}^H[k] (\mathbf{H}_{eq}[k] \mathbf{H}_{eq}[k]^H + \frac{N_o \Delta f}{P} \mathbf{I})^{-1}.$$

Thus in the SMBF scheme the precoding matrix that maps antenna ports to layers is different in each subcarrier. Finally, normalization and calculation of effective BF vectors proceeds as in the FMBF case, but with the effective vectors introduced in (1) taking different values for each subcarrier index k . For UL the same considerations regarding the transpose channel matrix at the receiver are applied.

This frequency-selective approach requires the estimation of effective channel coefficients for all pairs of co-existing users and for all subcarriers, which represents $K \times$ more feedback than in the FMBF scheme. In return, the frequency-selective approach guarantees an explicit suppression of the inter-user interference in all subcarriers. Potentially, this means that the SINR can be almost as high as the SNR without interference of a 1-layer system.

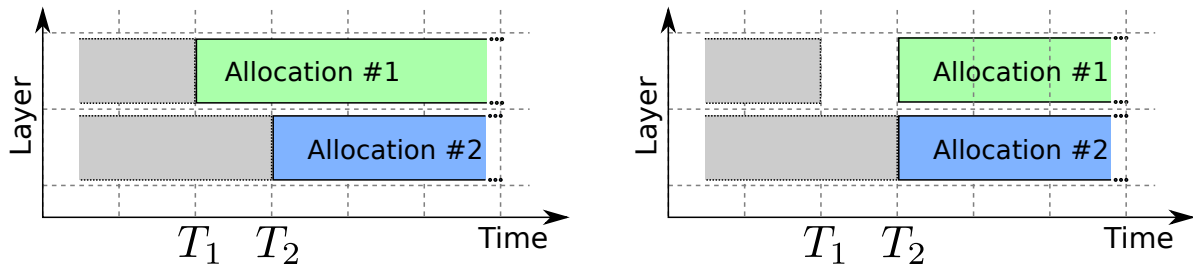
5) *Future Work*: We leave for future extensions of our work the study of MU-MIMO techniques that go beyond linear BF and independent encoding and decoding in each link. In recent years Non Orthogonal Multiple Access (NOMA) [30] has gained attention in the literature. NOMA schemes can be regarded as practical implementations of the classic capacity-achieving schemes for the MAC and broadcast channels in information theory [12]. As mentioned above, in UL the BS could decode all incoming transmissions jointly using Sphere Decoding [29] or

Successive Interference Cancellation. Conversely, in DL, the BS could jointly encode all transmitted signals using schemes inspired by Dirty Paper Coding, such as lattice-based Quantization Index Modulation [31]. Moreover, we also leave for future work the study of BF performance degradation due to quantization in the channel estimations versus the amount of incurred feedback overhead.

C. HBF and Scheduling Interaction

We assume that the scheduler allocates transmissions in a 2-dimensional resource grid combining TDMA and SDMA. All subcarriers in the same OFDM symbol are allocated to the same UE due to the fact that the BF system in mmWave is at least partially frequency-flat. The scheduler produces allocation decisions periodically for each slot of 14 symbols. The standard supports flexible configurations for allocating control information, i.e., the Physical Downlink Control Channel (PDCCH), in specific regions of each frame [16]. We assume a periodical control signaling scheme where, for every 14-symbol slot, the first symbol always contains the PDCCH. In the PDCCH, Downlink Control Information (DCI) control messages are delivered to all users. The symbols 2 to 13 are used for data and marked as “flexible,” meaning that they can be employed for DL or UL in any slot and this choice may vary over different slots. Finally, in the 14-th symbol in each slot the UEs transmit UL control information to the BS.

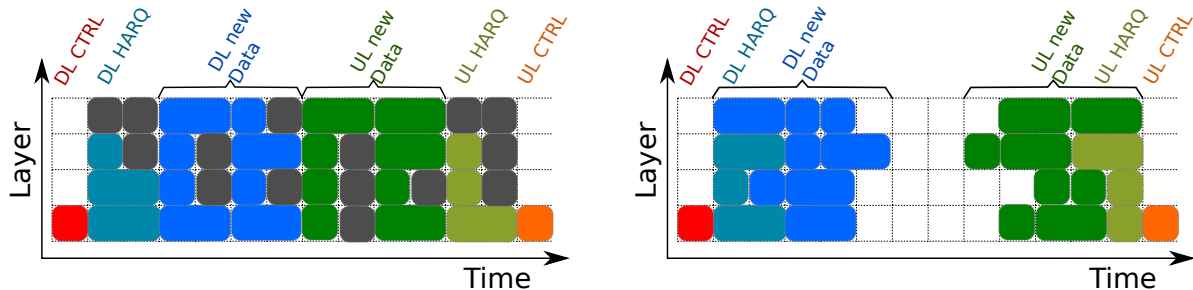
We assume perfect channel estimation and do not model the DMRSs explicitly. Since the smallest scheduling unit is a 2-symbol mini-slot with 1 DMRS symbol [14], in our model we assume that the minimum data allocation unit is reduced to 1 symbol of data transmission. We assume that allocated transmissions on different layers may present different start times (in symbol index units). Since each allocated transmission has only one front-loaded DMRS, the BF configuration of each transmission must be selected at the start of the transmission and cannot vary over the duration of the same transmission. This means that, for a pair of overlapping transmissions that start at different instants, the transmission that started first does not have information on the interference to design its BF (Fig. 1(a)). Therefore we assume that MMSE precoding/combining can only be applied to groups of allocations that start at the same time (Fig. 1(b)). Thus, there is a conflict between scheduling constraints and the applicability of the MMSE technique, as illustrated in Fig. 1. We consider two approaches illustrated in Fig. 2: the first can make full use of MMSE but imposes additional constraints on the scheduler leading to lower resource efficiency (Fig. 2(a)). In the second, we allow the scheduler to freely allocate resources



(a) BF conflict with different transmission start times: At T_1 allocation #1 does not observe reference signals from other layers. The BS cannot estimate (5) and use MMSE BF, falling back to CBF. When Allocation #2 starts at T_2 , the transmission of reference signals by Allocation #1 has already passed, so Allocation #2 must fall back to CBF as well. In addition, Allocation #1 cannot change its BF configuration at T_2 either. After T_2 , both allocations experience the interference power of a CBF scenario even though MMSE is supported by all devices.

(b) BF conflict with forced simultaneous transmission start: The transmission in the top layer ends at T_1 , but the scheduler leaves a padding symbol without signal and the new allocation starts at T_2 . When transmission in the bottom layer ends at T_2 , both layers start a new allocation simultaneously. Both allocations can observe the other's reference signals and estimate the off-diagonal coefficients of (5). MMSE BF can be employed and interference is reduced. However, the frame resource region corresponding to the time interval $T_2 - T_1$ in the top layer is wasted.

Figure 1. Example of MMSE BF conflict with different transmission start times.



(a) PMRS: The resources in gray are wasted as padding to guarantee that simultaneous allocations always start at the same time.

(b) AMRS: The resources in white are still available in the sense that, if more users were added, these resources could be assigned to them.

Figure 2. Examples of scheduler slot decisions with our two proposals

even with different start times among different transmissions, achieving a more efficient frame resource occupation (Fig. 2(b)), but causing a fraction of the transmission events to be unable to use MMSE for interference reduction.

1) *Padded mmWave RR Scheduler (PMRS)*: This scheduler guarantees that possibly overlapping transmissions start at the same time in all layers. To do so, given N_ℓ layers, N_s symbols and N_u total UEs, the scheduler first divides the subframe equally in $N_b = \lceil N_u/N_\ell \rceil$ ‘‘SDMA bundles.’’ Each SDMA bundle is defined as a collection of up to N_ℓ concurrent transmissions with

the same start time, but allocated to different layers. The bundles are further time-multiplexed using TDMA over the full subframe, where each bundle is exactly $N_a = \lfloor N_s/N_b \rfloor$ symbols long in time. All layers in the bundle start transmitting at the same time but may end transmitting at different times, according to the amount of data each UE has to transmit. Indeed, within each bundle, and for each layer, one UE is selected. If this UE demands fewer than N_a symbols, then its transmission ends before the end of the bundle, and the remaining symbols are left blank (padding). If $N_u > N_s \times N_\ell$, then some UEs are left unserved and become the first UEs in the list for the next subframe in a Round Robin (RR) fashion. $N_u < N_s \times N_\ell$ then all UEs get equal allocations.

PMRS follows a TDMA first and SDMA second principle, guaranteeing equal start times for all transmissions in a bundle. This guarantees that MMSE BF is always usable and interference will fully depend on the chosen BF scheme. The padding part in each bundle constitutes wasted symbols, and thus this scheduler may display some inefficiency in resource occupation.

2) *Asynchronous mmWave almost-RR Scheduler (AMRS)*: This scheduler, instead, does not waste any symbol in padding: given N_ℓ layers, N_s symbols and N_u total UEs, the scheduler first divides the users into N_ℓ “user groups.” Each user group is defined as a collection of UEs served in the same layer. The UEs of the same group are further time-multiplexed using an independent TDMA RR technique for each layer without taking into account decisions for other layers. If all UEs demand more resources than available, then each UE receives $\lfloor N_s N_\ell / N_u \rfloor$ symbols. However, UEs that demand fewer resources receive fewer symbols, their allocations end sooner, and the next UE in the same group begins its allocation immediately after, without any padding. Due to this, the start times of transmissions in one layer are determined independently of the start times of other layers. Notice that the UEs are divided among the layers using an integer division and, as a result, the number of UEs per layer may differ by one unit. Finally, UEs that cannot get any resources will be served first in the next slot. Since allocations may have different sizes we call the scheduler “almost-RR.”

The AMRS thus follows an SDMA first and TDMA second principle, guaranteeing that no symbols are left blank wastefully (i.e., when there is still demand). Free symbols may exist when the total demand of all UEs is lower than $N_s N_\ell$, but these symbols are not “blocked” and would be allocated if there were more demand. However, equal start times for all concurrent transmissions are not guaranteed. This means that MMSE BF is not fully used, and interference will be a mixture of two types of events: some allocations that just by chance happen to start

at the same time will still use MMSE, and some others that start at different times will not. Therefore, interference can be significantly greater than the best-case scenario of the selected BF scheme.

III. PERFORMANCE EVALUATION AND TRADEOFFS

This section presents a comprehensive performance evaluation of HBF schemes, evaluating the tradeoffs in the design of BF and scheduling strategies. We first describe the ns-3-based, end-to-end, full-stack simulator that we developed (Sec. III-A), and the simulation scenario (Sec. III-B), and then present results to compare the different BF strategies and scheduling schemes, according to different metrics and configurations of the protocol stack (Sec. III-C-Sec. III-G).

A. End-to-end Simulation of HBF for mmWave

We implemented an MU-MIMO HBF extension for the ns-3 mmWave module introduced in [11]. Earlier releases of this module were implemented using the NYU mmwave channel model [32], and adopting the LTE module in the official ns-3 release as a base [33]. Besides the bulk of the multiple-layer implementation, we have introduced adjustments that bring our simulation closer to the 3GPP 5G NR standards. Instead of the NYU channel model, we adopt the most recent 3GPP channel model implementation in ns-3 [34]. In addition, the OFDM resource grid parameters (bandwidth, subcarrier spacing, symbol duration, and number of slots per frame) reflect those of NR, as described in Sec. II-A and [14]. Notice that the ns-3 mmWave module assumes that control signaling is ideal and messages are never lost or corrupted.

In our implementation we have introduced modifications to numerous C++ classes in the ns-3 mmwave module. Notably, the antenna array module now supports multiple antenna ports, with different BF configurations. Moreover, the 3GPP channel model implementation has been extended to account for the multi-layer interference of Eq. (1) and Eq. (2), while the channel abstraction code and the physical layer implementation have been refactored to support multiple SDMA asynchronous layers (i.e., transmissions from a single entity). The BF strategies described in Sec. II-B have been implemented in a plug-and-play fashion, leveraging a novel, flexible BF module. Finally, we updated the ns-3 mmwave module MAC layer to support multiple asynchronous layers, by properly accounting for the mapping of upper layer PDUs to mmwave Transport Blocks on different antenna ports, the management of Hybrid Automatic Repeat reQuest (HARQ) retransmissions, the CQI estimation, and the control signaling. The MAC layer

Table I
DEVICE RADIO CONFIGURATION

	Transmit Power	Noise Figure	Number of Layers	Antenna Array
BS	30 dBm	5 dB	1 or 4	8×8 UPA
UE	30 dBm	5 dB	1	4×4 UPA

also features a plug-and-play implementation of the schedulers introduced in Sec. II-C, which is backward compatible and allows comparison with the other scheduling strategies implemented in the ns-3 mmWave module [11]. We refer the reader to the publicly available Github repository with the HBF extension for additional details.

B. Simulation Scenario

In the next few subsections we present different simulations pertaining to different aspects of the SDMA MU-MIMO mmWave system. For all simulations below, we consider a random mmWave cellular system with one BS located at the origin of the coordinates (0,0) with a height of 25 m, and 7 UEs located at random positions uniformly distributed in a disc of radius 100 m with a height of 1.6 m. We generate 20 such random deployments and average the results over the random UE locations and channels. We assume that due to the considerable pathloss in mmWave, inter-cell interference is severely attenuated and it is sufficient to simulate one cell. This is different from prior work that simulated 4G systems, where the simulators had to consider also a set of “encircling” neighboring cells to model interference realistically [35].

We configured the NR OFDM waveform with numerology $\mu = 2$, which corresponds to a subcarrier spacing of 60 kHz. The system operates at 28 GHz central frequency with a bandwidth of 198 MHz divided into 275 RBs, each including 12 subcarriers. There are 4 slots per subframe with duration $250 \mu\text{s}$, and the OFDM symbol duration is $17.85 \mu\text{s}$ including the CPs. We adopt the channel model described in 3GPP TR 38.901 [36] and consider the “Urban Macro” scenario. The radio hardware in the devices was configured with the parameters listed in Table I.

C. Comparison of BF Solutions

We compare the BF schemes discussed in Section II-B. To clearly highlight their impact on the physical layer, we use Radio Link Control (RLC)-Unacknowledged Mode (UM) (i.e., without RLC retransmissions), disable the HARQ retransmissions at the MAC layer, and use a low-traffic

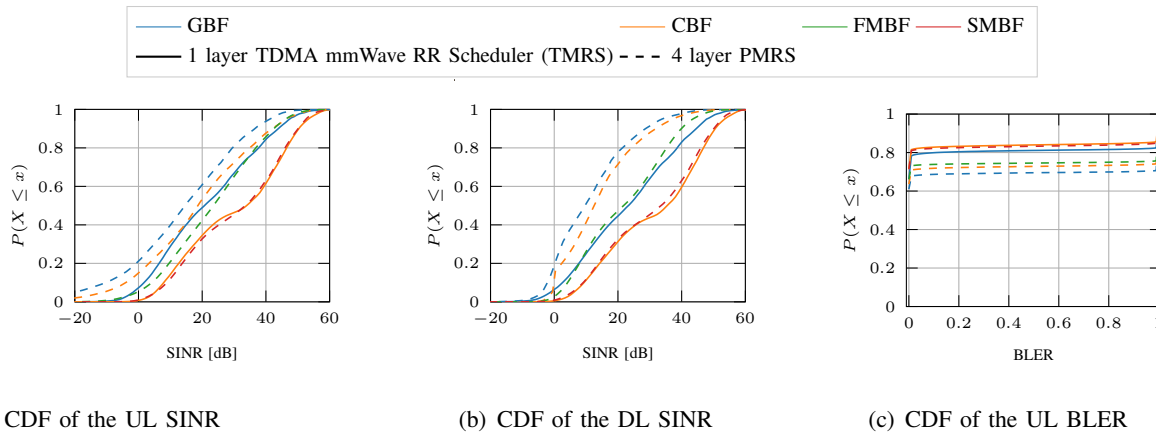


Figure 3. Comparison of the different BF schemes.

application in the UEs. This minimizes the difference between the statistics of the SINR and BLER perceived by the upper layers and the random distribution that generates these values at the channel model.

The low rate application is a constant traffic generator for downlink and uplink that produces a packet of 1500 bytes every 1500 μs , in each UE. Roughly speaking, when the Modulation and Coding Scheme (MCS) coding rate is greater than 3.64 bits per subcarrier, the 3300 subcarriers can carry a full packet in a single OFDM symbol. This means that, in every slot of 250 μs , the scheduler receives either a demand for at least ~ 14 symbols (i.e., each of 7 UEs requests one downlink and one uplink symbol), or none, in a regular pattern repeating every 6 slots. The scheduler has thus plenty of RBs to satisfy the traffic request, and, as discussed, there are no retransmissions. This makes it possible to probe the channel and BF scheme at a constant rate, and to measure the combined effect of the channel condition and BF scheme on physical layer performance metrics.

We represent the received UL SINR CDF for all transmission allocations in the simulation in Fig. 3(a). We compare 1 layer (solid) and 4 layer (dashed) cases. For the 1 layer case, we use the TMRS without SDMA capabilities that was implemented in the previous versions of the ns-3 mmWave module, with either GBF or CBF (MMSE BF is a multi-layer technique and would have no effect in the single layer case, behaving exactly as CBF). For the 4 layer case we consider the PMRS, so that all allocations use the specified BF scheme (i.e., the MMSE schemes never fall back to CBF, as discussed in Sec. II-B). We compare 4-layer GBF, CBF, FMBF, SMBF. Since there is no self-interference, in the 1-layer case the SINR is the same as the SNR, which is better with CBF than with GBF, consistently with our discussion in Sec. II-B. Moreover, if

we introduce 4 layers, but adopt any of the two single-layer BF schemes (GBF or CBF), the SINR drops significantly, with frequent -20 dB events. This confirms that the single-layer BF schemes do not perform well and *the use of multi-layer specific BF is necessary*. Adopting the FMBF scheme improves the SINR by a significant margin, but does not fully compensate the interference. As designed, the SMBF scheme does remove almost all interference, and its SINR CDF is nearly identical to that of the single-layer CBF case.

We represent the received DL SINR CDF in Fig. 3(b). The main difference with the UL case is that in DL the desired and interfering signals at each UE arrive through the same pathloss, and -20 dB SINR outages with 4-layer CBF rarely happen. On the other hand, the gap between the higher range of SINRs achieved with 4-layer CBF and 4-layer MMSE BF schemes is wider than in UL. Again the SMBF scheme removes virtually all interference and achieves an SINR distribution akin to that of a 1-layer CBF scenario; whereas the FMBF scheme achieves an intermediate SINR improvement.

Finally we depict the instantaneous BLER CDF for all UL transmissions in Fig. 3(c). Generally speaking, the BLER distribution is almost a step function: In each transmission, the Channel Quality Information (CQI) feedback is used to select the MCS such that the BLER would be 10^{-2} *if the reported channel stayed the same*. Therefore, we can define a ‘‘CQI outage’’ as the event that, at the moment of transmission, the channel has become much worse compared to when the CQI was reported, and the instantaneous BLER is $\simeq 1$. Fig. 3(c) shows that the instantaneous BLER is dominated by such outages, where most transmissions experience either $\text{BLER} \leq 10^{-2}$ or $\text{BLER} = 1$. The complement of this outage probability corresponds to the height of the flat region of the CDF curves. As we can see, 4-layer GBF and CBF have a much larger outage probability (lower step in the BLER CDF) and result in more severe BLER in the system. Again, we see that SMBF behaves almost as a 1-layer CBF situation, with the FMBF scheme in-between these two cases. We do not depict the DL BLER CDF due to space constraints, as its insights were identical.

In summary, the BF comparison shows that SMBF is necessary in the MU-MIMO 4-layer implementation in order to ensure that the physical layer achieves the same SINRs and BLER as in the 1-layer mmWave system with CBF. Moreover, the main differences between all BF schemes in this paper are that GBF performs worse than CBF for any number of layers and that FMBF offers some performance improvements without necessitating as much channel estimation overhead as SMBF.

D. Cross-layer BF and Scheduling Interactions

Next, we compare the performance of the scheduling algorithms introduced in Section II-C. To highlight the scheduler behavior with respect to the offered traffic, once again we use RLC-UM and disable the HARQ retransmissions at the MAC layer. However, differently from the previous section, we use high-traffic applications in the UEs to emphasize the effect that the scheduler has on the system performance.

Since we have already determined the best BF scheme for each number of layers, we consider four scenarios: the TMRS 1-layer scheduler with CBF, our proposed PMRS for both the 1-layer CBF and 4-layer SMBF configurations, and our proposed AMRS for 4-layers with SMBF. PMRS is designed for use with multiple layers, but since it forces all allocations to be of the same size in TDMA, its behavior when applied to the 1-layer case differs slightly from that of TMRS. For this reason we included an observation of the behavior of PMRS in the 1-layer case as well. AMRS, on the other hand, behaves exactly like TMRS if invoked on a 1-layer problem. Recall also that AMRS may assign allocations so that two overlapping transmissions do not start at the same time, and that in these events the SMBF scheme falls back to the behavior of a CBF scheme (see Fig. 1).

The high-rate application is a constant bit rate source that generates a packet of 1500 bytes every $150 \mu\text{s}$ in each UE, with a symmetric traffic in uplink and downlink. Recall that such packet can be sent with a single OFDM symbol (with 3300 subcarriers) if the MCS coding rate is greater than 3.64 bits/symbol. Overall, the traffic requests received by the scheduler saturate the RBs of the 1-layer case. Indeed, for every slot of $250 \mu\text{s}$, the scheduler always receives requests for at least ~ 23 symbols. In the 1-layer case there are 12 data symbols per slot, which are not enough to allocate all the demand. In the 4-layer case, there are 12×4 available data symbols, i.e., enough resources if most channels can support MCSs with rates greater than 1.82 bits/symbol.

Figure 4(a) reports the average DL and UL BLER for the four scheduler-BF pairs discussed above. As can be seen, AMRS displays a high UL BLER because it does not fully take advantage of the SMBF technique. The problem is more severe in UL because, as discussed in the previous section, the pathloss leads to more severe SINR drops (outages) in this direction than in DL. The BLER of PMRS with 4 layers is comparable to that of TMRS and PMRS with 1 layer, which is also consistent with the SINR plots discussed in the previous section.

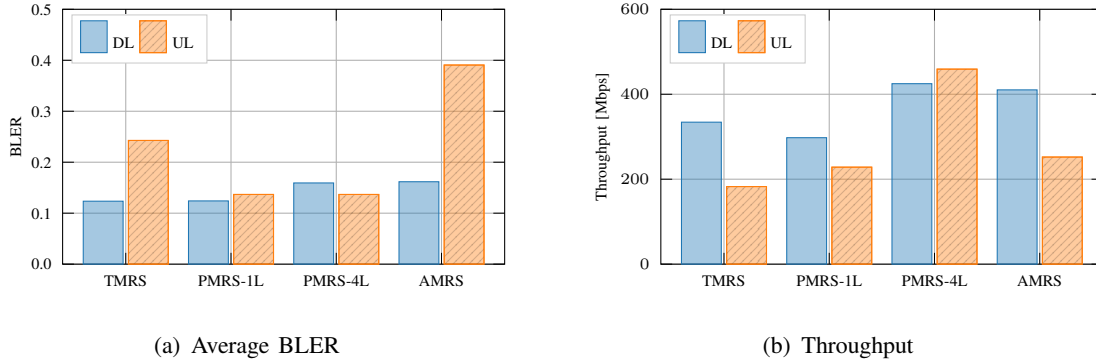


Figure 4. Comparison of the different scheduling strategies.

Figure 4(b) depicts the throughput, defined as total data received divided by total simulation duration. Since the nominal application rate is $\frac{7 \times 1500 \times 8}{150 \times 10^{-6}}$ bit/s, the maximum throughput is 560 Mbps. For TMRS, we see that the delivered throughput is around 330 Mbps in DL and 180 Mbps in UL, with significant asymmetry and much lower value than the offered traffic. This is consistent with the fact that the offered traffic greatly exceeds the number of data symbols of the 1-layer frame even with the best MCS. The same observation holds for the padding scheduler with 1-layer and CBF, although its DL/UL traffic is better balanced. In the 4-layer cases, the resources are not saturated by the source traffic, and the throughput with PMRS exceeds 420 Mbps in DL and 450 Mbps in UL. This shows the main advantage of incorporating SDMA MU-MIMO into mmWave networks, i.e., *an increase in the number of available RBs by a factor of N_{layers} allows the network to support much more traffic*. Particularly our simulation shows a delivered traffic that is $2 \times$ the capacity of the single-layer frame. As for AMRS, we see that it also supported over 410 Mbps of DL traffic successfully, but it only delivered around 250 Mbps of UL traffic. This is consistent with the observation that the UL BLER is high and the SINR can suffer significant outages when AMRS does not ensure that all layers start their transmissions at the same time, causing the SMBF scheme to fall back to CBF behavior. Therefore, despite the higher efficiency in the resource allocation, AMRS may perform worse than PMRS.

This section shows that the implementation of multi-layer SDMA MU-MIMO in the mmWave cellular system can greatly increase its capacity. However, to do so, attention must be paid to the inter-beam interference and scheduling conflict. In the previous section we had established that CBF in a multi-layer setting suffers occasional severe outages in UL. In this section we also show that this issue extends to SMBF used in combination with AMRS, since in this case the

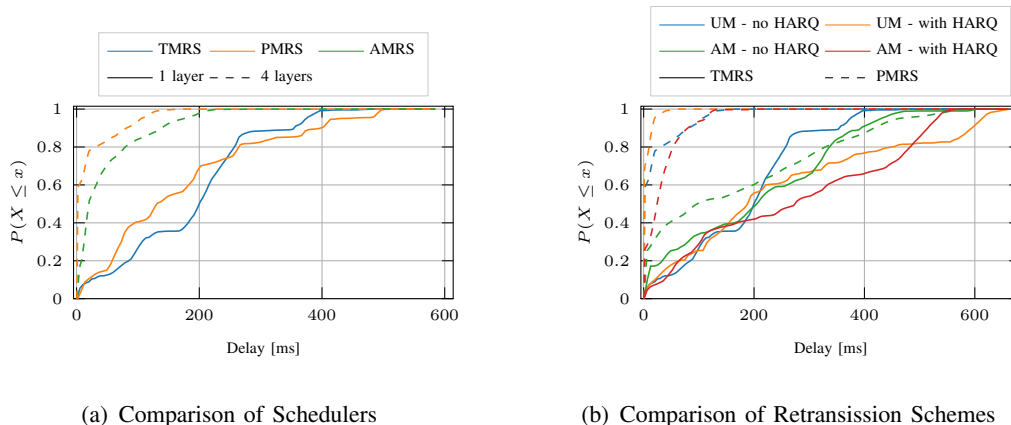


Figure 5. Delay in UL

BF scheme must occasionally fall back to CBF behavior.

E. Delay and Retransmissions

Capacity is not the only relevant network performance indicator. Some applications such as video streaming or eHealth are time constrained, whereas other applications such as smart grid and machine-type communications require strong reliability. In this section we leverage the end-to-end nature of our simulator to study the relation between the available retransmission schemes and delay in SDMA MU-MIMO mmWave NR networks. We note that delay measurements (which are taken at the Packet Data Convergence Protocol (PDCP) layer in the 3GPP stack) in simulations are affected by the so-called “survivor bias,” i.e., packets that are not delivered do not get their delay measured. For this reason unreliable transmission modes tend to display shorter delay statistics on the fewer packets successfully arriving, whereas the queuing and retransmission timeouts of reliable modes add to their total delay on a greater number of received packets. The RLC retransmission mode (i.e., RLC Acknowledged Mode (AM)) provides reliability on a much larger time scale than the MAC HARQ mechanism. The RLC “reordering timeout” is 10 ms, whereas the HARQ scheme retransmits immediately after a Negative Acknowledgment (NACK) is received. Since UL control information is processed at the end of every slot in our simulation, this makes the HARQ retransmission time less than 1 slot period or $250 \mu\text{s}$. For this reason we expect that RLC-AM will dominate the increase in delay caused by retransmissions.

Figure 5(a) compares the delay CDFs for different schedulers under the no retransmission configuration (RLC UM without HARQ), with the high traffic User Datagram Protocol (UDP) application presented in the previous section. We use the CDF instead of bar plots to highlight

the inverted-L shape of delay CDFs when most traffic is successfully delivered in the 4-layer configuration. With this, more than 75% of packets are received in under 20 ms, and more than 90% of packets are received under 100 ms. In a deadline constrained application, such as for example video with one frame every 20 ms, this means that 75% of the frames would be received on time and be displayed on screen (with no buffering). Turning our attention to the differences between AMRS and PMRS, the latter indeed guarantees a 10 ms deadline with probability 80% and a 100 ms deadline with probability 95%, which is much better than the deadline guarantees offered by AMRS. The 1-layer schemes, both TMRS and 1-layer-PMRS, do not display an inverse-L shaped CDF because the network capacity is exceeded by the applications. Instead, the delay CDF with 1-layer is roughly linear as many packets accumulated long times in the queue waiting to be transmitted.

Figure 5(b) displays the delay CDF using all four possible retransmission configurations for TMRS and 4-layer PMRS. Again we adopt the UDP high traffic application. Since the offered throughput exceeds the resources of the 1-layer frame the delays with TMRS present an almost-linear slope which is dominated by queue waiting time. On the other hand the PMRS cases present two-slope inverse-L shapes that are mostly driven by outages and retransmissions. The lowest delay 80%-tile is achieved by the RLC-UM with HARQ PMRS configuration, followed closely by the RLC-UM without HARQ PMRS configuration. It appears that HARQ retransmissions help improve delay, which suggests that their contribution to improve reliability compensates the small delays incurred by HARQ retransmissions. The CDFs for PMRS with RLC AM exhibit a very different behavior with or without HARQ retransmissions. Without HARQ, multiple AM retransmissions are needed, where each retransmission adds over 10 ms to the packet delivery delay. On the contrary, with HARQ most retransmissions take place at the MAC layer, with a short round-trip time, and RLC only needs to compensate for occasional HARQ failures. It is noteworthy that the delay CDF for the RLC AM without HARQ padding configuration looks similar to the 1-layer curves, which suggests that RLC retransmission queues are growing without bounds in this scenario. Regarding the differences in behavior between different retransmission configurations for TMRS, it seems that resource occupation dominates the delay since the 1-layer frame capacity is exceeded. That is to say, the RLC UM without HARQ 1-layer configuration does not add any resource demands besides that of applications, thus alleviating the queues, whereas the RLC AM with HARQ configuration adds resource demands to the scheduler on top of the demands already presented by the fresh packets, making the queues grow even longer and

the delay worsen.

The main conclusion of this section is that, since delay is strongly related to resource availability and queuing, the use of SDMA greatly increases the number of available resource blocks, permitting the schedulers to support larger traffic demands with low delay. Among the schedulers, PMRS offers an improved delay profile with respect to AMRS, but both are able to offer under 20 ms delay to a high percentage of the traffic. For intuitive reference, a video at 50 frames per second displays one frame every 20 ms, so this result is of the same order of magnitude as real-time multimedia applications. To introduce reliability, HARQ should be activated always first before considering the use of the RLC AM mode, as following the opposite order would cause too many retransmissions and delay at the RLC level.

F. Throughput vs Delay

This subsection further extends the scheduler comparison by considering joint throughput and delay results using the “full retransmission” scheme, i.e., the RLC AM mode with HARQ, versus the scenario “without retransmissions” consisting in using the RLC UM without HARQ retransmissions. As in the previous section, we consider a high-rate UDP application with 150 μ s inter-packet-interval and focus on the delay and throughput. We compare the default TMRS in the ns-3 mmWave module with 1 layer versus our PMRS and AMRS with 4 layers.

Figure 6(a) reports the mean UL delay vs throughput. Each point in the scatter cloud corresponds to one possible system configuration, with the best configuration corresponding to the top left corner, i.e., the highest throughput with the lowest delay. Recalling that the *offered* traffic is $7 \times 1500 \times 8/150 \times 10^{-6} = 560$ Mbps, we note that the 4-layer padding scheduler without retransmissions is the only one to deliver almost all the traffic. Surprisingly, activating the RLC AM mode with HARQ reduces the throughput, which means that the additional RB demand of the retransmissions overweighs the benefit of increased reliability. Since the offered traffic greatly exceeds the capacity of a 1-layer case, TMRS with 1-layer displays large delays (waiting in queues) and low throughput. This figure focuses to the UL performance, in which AMRS suffers occasional outage problems, and hence its throughput and delay are much worse than PMRS.

Figure 6(b), instead, reports the same metrics for the DL traffic. The major difference with the UL case is that now AMRS performs much better. Indeed, with retransmissions enabled, AMRS displays the highest throughput at the cost of a slightly higher delay (due to the RLC

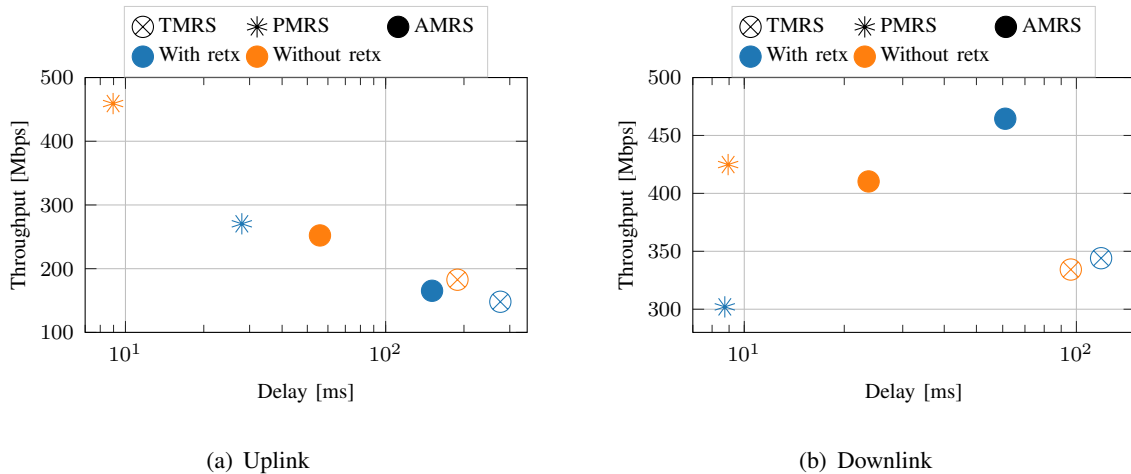


Figure 6. Comparison of the different scheduling strategies.

AM retransmission timer). On the other hand, PMRS displays a significant drop in throughput with retransmissions versus the case without them. In this case, indeed, the padding brings the resource occupation close to saturation and the retransmissions, which increase the resource demand, saturate the capacity and cause a net decrease in throughput. AMRS, on the other hand, is not affected by this issue (at least not yet, with this source rate), as it is more efficient in allocating resources.

The results in this section highlight the importance of a full-stack, end-to-end performance evaluation. Indeed, the evaluation of the BLER and SINR in Sec. III-D seemed to suggest that AMRS always performed equal or worse than PMRS. However, in DL, the BLER penalty of AMRS can be compensated using retransmissions, and, overall, the more efficient resource allocation yields an improved throughput. Conversely, since PMRS wastes some frame resources, the activation of retransmissions worsens the cell saturation and penalizes its throughput instead of helping it. Nonetheless, in UL AMRS severely underperforms PMRS. This suggests that different scheduling principles could be adopted for the two directions.

G. Performance with different traffic sources

Finally, we compare the system performance under three different applications and transport layer configurations, and investigate the relation between the application traffic and the scheduler. The first two applications are those considered in Sec. III-C and Sec. III-D, i.e., a constant bitrate source that generates a packet of 1500 bytes every 1500 or 150 μ s. In this case, the transport layer is UDP (thus they will be referred to as *UDP slow* and *UDP fast*, respectively). Finally, we also

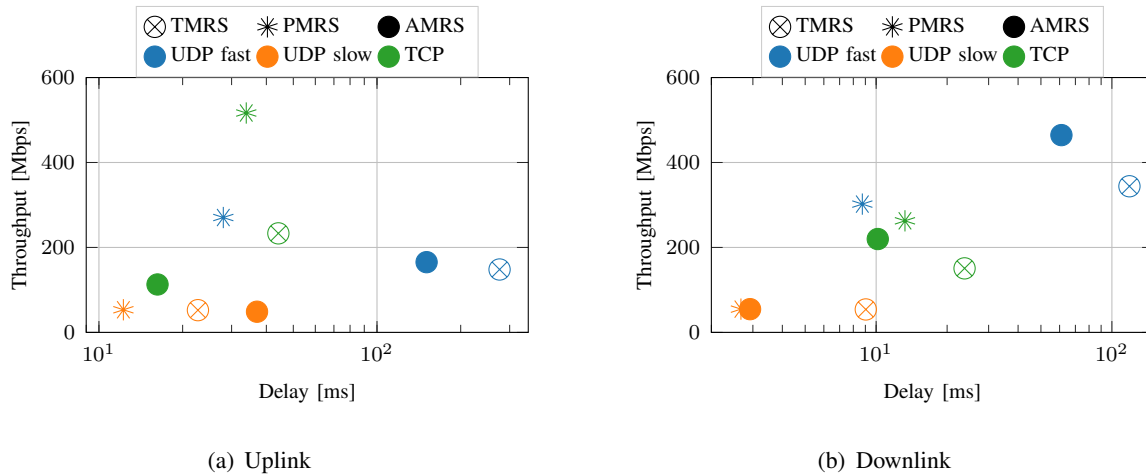


Figure 7. Comparison of different applications.

profile the performance with a full buffer application that relies on TCP at the transport layer, to adjust the offered traffic to the maximum supported by the network. We consider retransmissions in the RLC and MAC layers to obtain similar reliability in the applications over UDP as in the application over TCP.

Figure 7(a) represents the UL delay vs throughput for all three applications and all three scheduling solutions. Since in the UDP slow application (in yellow) the offered traffic is much lower than the potential cell capacity, almost all source rate is successfully delivered by all schedulers (about 56 Mbps). In addition, PMRS displays the lowest delay, followed by TMRS, with AMRS offering the worst UL delay. As discussed throughout the prior sections this is because of the occasional events where AMRS suffers deep SINR outages in UL. In the UDP fast application (in blue) the traffic sources offer 10 \times more throughput, which is almost fully delivered using PMRS. TMRS and AMRS do not deliver all the UL traffic for different reasons. While in TMRS this is due to the limited resources of the 1-layer frame, in AMRS the reason is the high BLER due to the occasional outages. Since the UDP fast application does not adjust its transmission queues the delay in these two schedulers increases significantly. Finally, for the TCP application (in green), PMRS offers the best performance achieving about 560 Mbps. TMRS has limited resources in the 1-layer frame and hence the throughput is less than half, but the delay is tolerable under 50 ms. Finally AMRS achieves a very low rate, which can be explained by the TCP rate control responding too strongly to the occasional SINR outages, which produce packet losses that trigger the TCP congestion control, reducing the transmission window.

Similarly, Fig. 7(b) represents the DL delay vs throughput for all three applications and all

three scheduling solutions. As in the previous figures, the main difference is that AMRS performs much better in DL than in UL. For the UDP slow application we still see that all the traffic is delivered, but the source rate is small. In DL the delay is much lower and similar between the two 4-layer schedulers (under 3 ms), whereas the delay of TMRS is a bit higher but still under 10 ms. For the UDP fast application AMRS turns out to be the best in terms of total DL throughput, albeit with considerable more delay than PMRS. TMRS displays high delay and limited throughput due to the lack of resources of the 1-layer frame. The throughput with PMRS is about half as much as with AMRS, but with much lower delay. Notably, the throughput-delay behavior of PMRS with UDP fast is similar to that of the TCP application with either 4-layer scheduler. As the TCP rate adaptation reduces the transmission window when certain timers expire, its delay is under 30 ms for all schedulers, but the achieved rate with such delay varies. PMRS offers the best TCP throughput with under 15 ms delay, followed closely by AMRS scheduler. Finally TMRS achieves the worst TCP throughput, with the highest delay, due to the limited resources of the 1-layer frame.

The main conclusion of this section is that the MU-MIMO system performance depends significantly on the offered traffic. For a lightly loaded cell with fixed traffic, all the configurations discussed offer a satisfactory behavior, whereas strong trade-offs between delay and throughput emerge in an over-loaded cell with fixed traffic. Moreover the different scheduling algorithms diverge significantly in their response to the over-loaded scenario, with PMRS displaying better delay generally, AMRS displaying more DL rate with some delay increase, and TMRS being overwhelmed by the traffic. Applications on top of TCP are more sophisticated and adapt their rates to the network. In this case the severe delays of the over-loaded scenario are avoided by the rate adjustment, which converges to a significantly larger rate for the 4-layer models compared to the 1-layer baseline. Generally PMRS offers consistently good performance in both UL and DL, whereas AMRS is a great scheme in DL but has severe shortcomings in UL.

IV. CONCLUSIONS

In this paper we have studied the simulation of MU-MIMO HBF implementations for 3GPP NR mmWave cellular systems. We have shown that by supporting multiple transmission layers simultaneously, the system capacity is greatly increased. Moreover, by associating each frequency-flat BF vector to a separate antenna port, the signal processing involving large arrays characteristic of mmWave systems can be handled in a space of reduced dimensions. In addition, by considering

a linear matrix mapping logical transmission layers to physical antenna ports, it is possible to leverage the advantages of MU-MIMO signal processing techniques in order to alleviate the inter-user interference and improve the SINR. We have shown that this is indeed necessary, as the SINR would degrade significantly if we merely used separate analog beams for each user without MU-MIMO-aware HBF. With regard to control overhead, we present a frequency-flat MMSE BF scheme with reduced feedback that achieves a partial interference removal, and a frequency-selective MMSE BF scheme with significantly more feedback that achieves almost complete interference removal.

We have revealed a trade-off between the design of MU-MIMO schedulers and the BF problem. Particularly, due to the characteristics of channel estimation in NR, only coexisting allocations that start at the same time are able to employ MU-MIMO-aware HBF techniques in order to reduce the interference. This raises a conflict between interference mitigation and RB allocation, as some wasteful padding symbols are needed to enforce the constraint that all allocations start at the same time. We have implemented two types of schedulers, one with padding and one that permits asynchronous transmissions and wastes no resources. We have shown through simulation that the latter scheduler leads to system performance degradation on average, although during its operation the events with too much interference are only occasional and may be compensated with adequate retransmission schemes, at the expense of some delay increase.

We have studied the relation between the system throughput and delay performance indicators, the application data rates, and this scheduler-BF trade-off. In general the use of the padding scheduler displayed the most consistent behavior, achieving satisfactory delays with much higher throughput than a baseline 1-layer system in both DL and UL. On the other hand, the asynchronous scheduling approach cannot yet be fully discarded, as we have shown that it offers even greater throughput in some very specific DL scenarios. In UL, due to the severe outages caused by large differences of pathloss between users, the asynchronous scheduling approach performs poorly.

REFERENCES

- [1] ITU-R, “IMT Vision - Framework and overall objectives of the future development of IMT for 2020 and beyond,” Recommendation ITU-R M.2083, Sep. 2015.
- [2] F. Boccardi, R. W. Heath Jr, A. Lozano, T. L. Marzetta, and P. Popovski, “Five Disruptive Technology Directions for 5G,” *IEEE Communications Magazine*, vol. 52, no. 2, pp. 74–80, Feb. 2014.
- [3] M. Giordani, M. Polese, M. Mezzavilla, S. Rangan, and M. Zorzi, “Toward 6G Networks: Use Cases and Technologies,” *IEEE Communications Magazine*, vol. 58, no. 3, pp. 55–61, Mar. 2020.

- [4] 3GPP, “NR and NG-RAN Overall Description,” TS 38.300 (Rel. 15), 2018.
- [5] —, “New WID on extending current NR operation to 71 GHz,” Qualcomm, RP-193229 - 3GPP TSG RAN Meeting 86, Dec. 2019.
- [6] S. Rangan, T. S. Rappaport, and E. Erkip, “Millimeter-Wave Cellular Wireless Networks: Potentials and Challenges,” *Proceedings of the IEEE*, vol. 102, no. 3, pp. 366–385, Mar. 2014.
- [7] S. Sun, T. Rappaport, R. Heath, A. Nix, and S. Rangan, “MIMO for Millimeter-Wave Wireless Communications: Beamforming, Spatial Multiplexing, or Both?” *IEEE Communications Magazine*, vol. 52, no. 12, pp. 110–121, Dec. 2014.
- [8] A. Alkhateeb, O. E. Ayach, G. Leus, and R. W. Heath, “Hybrid Precoding for Millimeter Wave Cellular Systems with Partial Channel Knowledge,” in *Proc. Information Theory and Applications Workshop (ITA)*, San Diego, CA, USA, Feb. 2013.
- [9] S. Mondal and J. Paramesh, “A Reconfigurable 28-/37-GHz MMSE-Adaptive Hybrid-Beamforming Receiver for Carrier Aggregation and Multi-Standard MIMO Communication,” *IEEE Journal of Solid-State Circuits*, vol. 54, no. 5, pp. 1391–1406, May 2019.
- [10] M. Giordani, M. Polese, A. Roy, D. Castor, and M. Zorzi, “A Tutorial on Beam Management for 3GPP NR at mmWave Frequencies,” *IEEE Communications Surveys Tutorials*, vol. 21, no. 1, pp. 173–196, Sep. 2019.
- [11] M. Mezzavilla, M. Zhang, M. Polese, R. Ford, S. Dutta, S. Rangan, and M. Zorzi, “End-to-End Simulation of 5G mmWave Networks,” *IEEE Communications Surveys & Tutorials*, vol. 20, no. 3, pp. 2237–2263, Apr. 2018.
- [12] A. Goldsmith, S. A. Jafar, N. Jindal, and S. Vishwanath, “Fundamental Capacity of MIMO Channels,” *IEEE Journal on Selected Areas in Communications*, vol. 21, pp. 684–702, Nov. 2002.
- [13] T. L. Marzetta, “How Much Training is Required for Multiuser MIMO?” in *2006 Fortieth Asilomar Conference on Signals, Systems and Computers*, Pacific Grove, CA, USA, Nov. 2006, pp. 359–363.
- [14] 3GPP, “NR; Physical channels and modulation, v16.1.0,” TS 38.211, Apr. 2020.
- [15] —, “NR; Multiplexing and channel coding, v16.1.0,” TS 38.212, Apr. 2020.
- [16] —, “NR; Physical layer procedures for control, v16.1.0,” TS 38.213, Apr. 2020.
- [17] B. Mondal, V. Sergeev, A. Sengupta, G. Ermolaev, A. Davydov, E. Kwon, S. Han, and A. Papathanassiou, “MU-MIMO and CSI Feedback Performance of NR/LTE,” in *53rd Annual Conference on Information Sciences and Systems (CISS)*, Baltimore, MD, USA, USA, 2019.
- [18] R. W. Heath, N. González-Prelcic, S. Rangan, W. Roh, and A. M. Sayeed, “An Overview of Signal Processing Techniques for Millimeter Wave MIMO Systems,” *IEEE Journal of Selected Topics in Signal Processing*, vol. 10, no. 3, pp. 436–453, Apr. 2016.
- [19] F. Sahrabi and W. Yu, “Hybrid Analog and Digital Beamforming for mmWave OFDM Large-Scale Antenna Arrays,” *IEEE Journal on Selected Areas in Communications*, vol. 35, no. 7, pp. 1432–1443, July 2017.
- [20] M. N. Kulkarni, A. Ghosh, and J. G. Andrews, “A Comparison of MIMO Techniques in Downlink Millimeter Wave Cellular Networks With Hybrid Beamforming,” *IEEE Transactions on Communications*, vol. 64, no. 5, pp. 1952–1967, May 2016.
- [21] D. Moltchanov, A. Ometov, P. Kustarev, O. Evsutin, J. Hosek, and Y. Koucheryavy, “Analytical TCP Model for Millimeter-Wave 5G NR Systems in Dynamic Human Body Blockage Environment,” *Sensors*, vol. 20, no. 14, p. 3880, Jul. 2020.
- [22] S. Choi, J. Song, J. Kim, S. Lim, S. Choi, T. T. Kwon, and S. Bahk, “5G K-SimNet: End-to-End Performance Evaluation of 5G Cellular Systems,” in *16th IEEE Annual Consumer Communications Networking Conference (CCNC)*, Las Vegas, NV, USA, USA, Jan. 2019.

- [23] S. Sur, I. Pefkianakis, X. Zhang, and K.-H. Kim, "WiFi-Assisted 60 GHz Wireless Networks," in *Proc. of ACM MobiCom*, Snowbird, Utah, USA, 2017, pp. 28–41.
- [24] M. Zhang, M. Polese, M. Mezzavilla, J. Zhu, S. Rangan, S. Panwar, and M. Zorzi, "Will TCP Work in mmWave 5G Cellular Networks?" *IEEE Communications Magazine*, vol. 57, no. 1, pp. 65–71, Jan. 2019.
- [25] C. Slezak, M. Zhang, M. Mezzavilla, and S. Rangan, "Understanding End-to-End Effects of Channel Dynamics in Millimeter Wave 5G New Radio," in *IEEE 19th International Workshop on Signal Processing Advances in Wireless Communications (SPAWC)*, Kalamata, Greece, Jun. 2018, pp. 1–5.
- [26] S. Han, C. I. Z. Xu, and C. Rowell, "Large-scale Antenna Systems with Hybrid Analog and Digital Beamforming for Millimeter Wave 5G," *IEEE Communications Magazine*, vol. 53, no. 1, pp. 186–194, Jan. 2015.
- [27] S. Dutta, C. N. Barati, D. Ramirez, A. Dhananjay, J. F. Buckwalter, and S. Rangan, "A Case for Digital Beamforming at mmWave," *IEEE Transactions on Wireless Communications*, vol. 19, no. 2, pp. 756–770, Feb. 2020.
- [28] 3GPP, "NR; User Equipment (UE) radio transmission and reception; Part 2: Range 2 Standalone, v16.3.1," *TS 38.102-2*, Apr. 2020.
- [29] U. Fincke and M. Pohst, "Improved methods for calculating vectors of short length in a lattice, including a complexity analysis," *Mathematics of computation*, vol. 44, no. 170, pp. 463–471, Apr. 1985.
- [30] Y. Saito, Y. Kishiyama, A. Benjebbour, T. Nakamura, A. Li, and K. Higuchi, "Non-Orthogonal Multiple Access (NOMA) for Cellular Future Radio Access," in *IEEE 77th Vehicular Technology Conference (VTC Spring)*, Dresden, Germany, Jun. 2013, pp. 1–5.
- [31] B. Chen and G. W. Wornell, "Quantization index modulation: a class of provably good methods for digital watermarking and information embedding," *IEEE Transactions on Information Theory*, vol. 47, no. 4, pp. 1423–1443, May 2001.
- [32] M. K. Samimi and T. S. Rappaport, "3-D Millimeter-Wave Statistical Channel Model for 5G Wireless System Design," *IEEE Transactions on Microwave Theory and Techniques*, vol. 64, no. 7, pp. 2207–2225, Jul. 2016.
- [33] "ns-3 — a discrete-event network simulator for internet systems," <https://www.nsnam.org/>, accessed: 2020-06-22.
- [34] T. Zugno, M. Polese, N. Patriciello, B. Bojovic, S. Lagen, and M. Zorzi, "Implementation of A Spatial Channel Model for ns-3," in *Proceedings of the 2020 Workshop on ns-3 (WNS3)*, Gaithersburg, MD, USA, Jun. 2020.
- [35] F. Gómez-Cuba and F. J. González-Castaño, "Improving third-party relaying for LTE-A: A realistic simulation approach," in *IEEE International Conference on Communications (ICC)*, Sydney, NSW, Australia, Jun. 2014.
- [36] 3GPP, "Study on channel model for frequencies from 0.5 to 100 GHz," *TR 38.901*, v15.0.0, Jun. 2018.